Flash-back, blow-off, and symmetry breaking of premixed conical flames

Christopher M Douglas, Wolfgang Polifke, Lutz Lesshafft

Highlights

Flash-back, blow-off, and symmetry breaking of premixed conical flames

Christopher M. Douglas, Wolfgang Polifke, Lutz Lesshafft

- Relates axisymmetric flash-back and blow-off phenomena to saddle–node bifurcations of a coupled flame/flow model.
- Identifies polyhedral and tilted flames as manifestations of three-dimensional global instabilities that emerge at low Lewis numbers and high Damköhler numbers, respectively.

Flash-back, blow-off, and symmetry breaking of premixed conical flames

Christopher M. Douglas[a], Wolfgang Polifke[b], Lutz Lesshafft[a]

[a] *LadHyX, CNRS, École Polytechnique, Institut Polytechnique de Paris, 91120 Palaiseau, France*
[b] *Technische Universität München, 80333 Munich, Germany*

Abstract

Hydrodynamic and thermal-diffusive effects subject premixed flames to intrinsic instabilities that strongly influence their shape and propagation/stabilization characteristics. However, the interaction and coupling of intrinsic flame dynamics with background flow gradients and boundary conditions remain poorly understood. This paper presents a global nonlinear bifurcation analysis of burner-stabilized laminar premixed conical flames with varying reaction rates and reactant diffusivities, respectively parameterized by the Damköhler number Da and the Lewis number Le. Using a dimensionless formulation of the reacting, weakly-compressible Navier–Stokes equations, the dynamics of flash-back, blow-off, and cellular instability are explored in a fully-coupled framework. Our analysis identifies steady conical flame states over a finite range of Da and Le, limited by saddle–node bifurcations corresponding to spontaneous blow-off of the axisymmetric flame below a Le-dependent lower critical Da value and spontaneous boundary-layer flash-back beyond a higher critical Da value. Furthermore, the analysis reveals that the conical flame loses its axisymmetry via circle–pitchfork bifurcations as Le or Da decrease or increase beyond respective critical values. These bifurcations are shown to correspond to stationary three-dimensional global modes describing steady polyhedral or tilted flame structures, each associated with distinct azimuthal periodicities.

Keywords: Bifurcation analysis, Flash-back, Blow-off, Hydrodynamic instability, Thermal-diffusive instability, Polyhedral flames

Novelty and Significance Statement

This work presents a bifurcation analysis of laminar premixed conical flames within a fully-coupled flame/flow model. By considering variations in reaction rate and reactant diffusivity, the analysis identifies saddle–node bifurcations corresponding to spontaneous flash-back and blow-off of the axisymmetric flame. It also identifies axisymmetry breaking bifurcations associated with transitions to steady three-dimensional polyhedral and tilted flame states. These global instabilities indicate that hydrodynamic and thermal-diffusive effects strongly influence a flame's steady structure in the azimuthal dimension even when no instabilities appear in the plane of symmetry. As such, future analyses of flame dynamics should rule out symmetry-breaking behaviors before adopting a two-dimensional computational framework.

Author Contributions

C.D. developed the methodology, performed the calculations, analyzed and interpreted the results, created the figures, and drafted the manuscript. W.P. and L.L. assisted with interpretation of results, contributed to the final design of the figures and text, and supervised the project.

1. Introduction

Concerns surrounding climate change and energy security are motivating major efforts to replace fossil fuel with renewable, carbon-neutral fuels. A primary contender in this space is hydrogen, which can be generated sustainably via electrolysis using excess renewable power. However, hydrogen fuel is associated with many unique challenges in the lean-premixed operation mode demanded by modern emissions regulations [1]. One key issue in this context is the relative proclivity of hydrogen flames toward intrinsic flame instability in comparison to hydrocarbon fuels such as methane. These instabilities may lead to wrinkling of the flame front into cellular patterns, significantly increasing the flame's surface area and, therefore, its overall propagation velocity. Further, premixed flames are not passive fronts, but are strongly coupled to the flow within which they are embedded. Lean hydrogen flames in particular are remarkably sensitive to flame curvature and stretch due to hydrodynamic strain. Such couplings lead to complex system behavior that is not generally identifiable when considering the hydrodynamics and thermodynamics of a reacting flow system in a decoupled manner. Therefore, a

key contribution of this study will be to consider such behavior in a simple, but fully-coupled, reactive flow model.

Laminar flame instabilities play a crucial role in the propagation of turbulent flames, and their fundamental relevance to practical combustion problems is well-established [2, 3]. The mechanistic understanding of intrinsic flame instability is rooted in analytical results obtained from perturbation analysis of thin, freely-propagating planar flames. For example, the *thermal-diffusive* mechanism [4, 5] amplifies a range of small-scale flame wrinkles when the deficient reactant's mass diffusivity exceeds the thermal diffusivity of the mixture, i.e. at sub-unity Lewis number ($Le < 1$). Conversely, the *hydrodynamic* mechanism, which occurs due to thermal expansion [6, 7], amplifies flame wrinkles even when the mass and thermal diffusivities are equal ($Le = 1$). Additional mechanisms such as flame stretch [8, 9] and heat loss [10, 11] also significantly contribute to the wave dispersion behavior, interacting to determine the growth rate for a given wrinkle length-scale [3, 12, 13]. Such amplified wrinkles typically evolve into finite amplitude cellular patterns along the flame front that may directly compete with turbulence to control flame propagation behavior [14].

Though much of the community's efforts toward understanding flame instabilities is focused on geometrically simple arrangements involving freely-propagating flat or spherical flames, these dynamics also appear in anchored flames, such as conical (or "Bunsen") flames. When the flame front is stabilized by shear and/or confinement, additional thermal-diffusive and hydrodynamic effects related to the background strain and boundary conditions arise that further complicate the flame dynamics and affect its structure [8, 15]. A striking example of this, which will be explored in this study, is the spontaneous emergence of azimuthally-periodic polyhedral shapes from conical Bunsen flames.

Polyhedral Bunsen flames were first reported by Smithells and Ingle [16] in rich benzene, pentane, and hexane mixtures and subsequently described and analyzed in progressively greater detail in a variety of experimental circumstances featuring sub-unity Lewis numbers [17, 18, 19, 20, 21, 22]. Unlike free flat or spherical flames, Bunsen flames experience significant heat losses to the burner and are strained by local velocity gradients that induce negative stretch (compression) near the flame tip and positive stretch near the flame foot. These complications induce strong sensitivities of Bunsen flame properties on the specific burner geometry [19], the flow rate [17], and the fuel composition [20]. Such experiments demonstrate that chemistry, aero-

dynamics, and heat transfer all significantly affect the flame's axisymmetric or polyhedral structure and, in the latter case, determine the number of faces and whether the flame is stationary, rotates smoothly, or changes shape chaotically in time.

Perhaps because of this complexity, quantitative theoretical understanding about polyhedral flame behaviors is quite limited. Nonetheless, a handful of reduced order models have been put forward based on variations of the Kuramoto–Sivashinsky flame equation [5]. For example, Buckmaster [23] proposed a weakly-nonlinear model, further developed by Olagunju and Matkowsky [24], to explain how interactions of two linearly unstable polyhedral flame shapes could lead to apparent rotation of cellular structures via transient mode switching. This proposal has since been disputed by Michelson [25] and Class [26], who argue based on slightly different ODE models that the onset of polyhedral flame rotation instead follows a primary bifurcation directly from an axisymmetric state to a rotating state. Nonetheless, Gutman *et al.* [27] were unable to find any rotating solutions in their simulations, suggesting such solutions might be unstable. Using Frankel's coordinate-free variation of the flame equation [28], Denet [29] performed further simulations in a PDE framework. His results, which also did not identify rotating flames, revealed significant sensitivities to flame holding and boundary layer thickness parameters in a qualitatively similar manner to experiments [19]. Overall, however, these studies are all based on heavily simplified flame models that neglect density changes, stretch effects, flame thickness effects, and several other fundamental aspects of reacting flow.

The purpose of this paper is to consider the dynamics of conical laminar flames from a more comprehensive model that preserves the strongly nonlinear flame-flow coupling known from first principles. The remainder of this paper is organized as follows. In §2, we describe the configuration (§2.1) and formulation (§2.2) of the model and outline the bifurcation theory (§2.3) and numerics (§2.4) used in the analysis. We then present and discuss the main results of our study in §3. The results begin with an overview of the model's axisymmetric behavior in the case of varying Damköhler number (Da) and unity Le (§3.1.1) as well as the converse case of variable Le and constant Da (§3.1.2). From here, we extend the analysis to consider non-axisymmetric effects over the Da–Le plane in §3.2. Finally, we close with a summary of this investigation and some concluding remarks in §4.

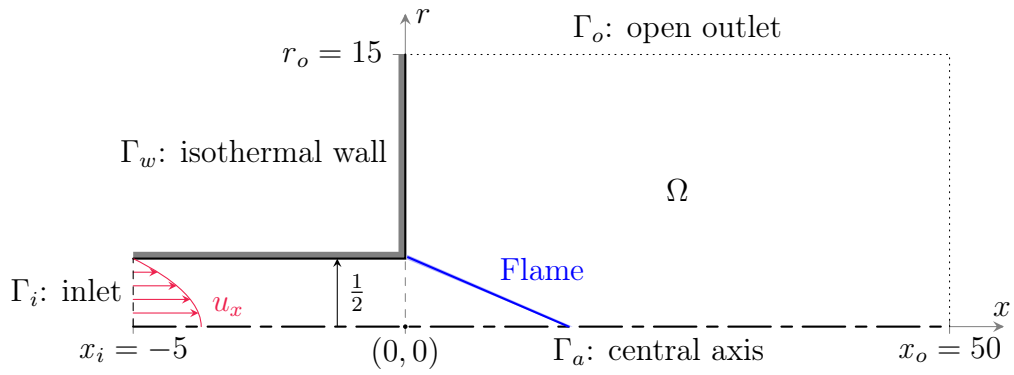

Figure 1: Meridional schematic of the axisymmetric burner configuration (not to scale).

2. Model

2.1. Burner Configuration

This study models a round jet of premixed reactants undergoing combustion while venting from a long pipe into a large semi-open domain. The resulting laminar conical flame, which we refer to as a Bunsen flame, is considered in a cylindrical coordinate system defined by $\boldsymbol{x} = (x, r, \theta)$, as shown in Figure 1. The boundary conditions are specified in Table 1 and described below. The inflow condition along the inlet Γ_i is a Poiseuille velocity profile with a uniform temperature and reactant concentration. The boundary Γ_w along the inlet pipe and dump plane is an isothermal no-slip wall held at the inlet reactant temperature. The central axis Γ_a is a symmetry boundary where three-dimensional continuity conditions are enforced for each azimuthal Fourier component m of each flow variable (see section 2.3 below). Finally, the open boundary Γ_o along the lateral and downstream edges of the domain is modeled with free-outflow conditions. Throughout this paper, all quantities are expressed as dimensionless numbers scaled by the pipe diameter D, the volume-averaged velocity of the incoming flow U, and the reference physical properties of the incoming reactants.

2.2. Governing Equations

The dimensionless, reactive equations governing the evolution of the present flame/flow system are derived in Appendix A from the full conservation equations given by Poinsot & Veynante [30, Ch. 1]. Nonetheless, a number of simplifying approximations are invoked to obtain the form used here. Only

Table 1: List of boundary conditions. Here, $\boldsymbol{n}$ is the unit normal vector along the border.

Name		**Constraints**
Inlet, Γ_i:		$u_x = 2 - 8r^2, \quad u_r = u_\theta = 0, \quad Y = T = 1,$
Wall, Γ_w:		$u_x = u_r = u_\theta = 0, \quad \boldsymbol{n} \cdot \boldsymbol{\nabla} Y = 0, \quad T = 1,$
Axis, Γ_a:	$m = 0$:	$\partial_r u_x = 0, \quad u_r = u_\theta = 0, \quad \partial_r Y = \partial_r T = 0,$
	$\lvert m \rvert = 1$:	$u_x = 0, \quad \partial_r u_r = \partial_r u_\theta = 0, \quad Y = T = 0,$
	$\lvert m \rvert \geq 2$:	$u_x = u_r = u_\theta = Y = T = 0,$
Open, Γ_o:		$Re^{-1} \boldsymbol{n} \cdot \boldsymbol{\nabla} \boldsymbol{u} - p \boldsymbol{n} = 0, \quad \boldsymbol{n} \cdot \boldsymbol{\nabla} Y = \boldsymbol{n} \cdot \boldsymbol{\nabla} T = 0.$

the essential aspects of this reduction are summarized here, as complete details are given in Appendix A. A low Mach number approximation is used to simplify acoustics and focus on thermal compressibility effects. Chemistry is modeled using Arrhenius' law for a single-step, irreversible, fuel- or oxidizer-limited (very lean or rich, respectively) reaction. Thermal and mass diffusion are modeled by Fick's Law, with temperature-dependent diffusivity (and viscosity) coefficients modeled by a power-law relation with an exponent of $2/3$. The resulting dimensionless system governing the velocity, deficient reactant mass fraction, temperature, and pressure fields ($\boldsymbol{u}$, Y, T, and p, respectively) is,

$$\frac{1}{T}\left(\frac{\partial \boldsymbol{u}}{\partial t} + \boldsymbol{u} \cdot \boldsymbol{\nabla} \boldsymbol{u}\right) = -\boldsymbol{\nabla} p + \frac{1}{Re} \boldsymbol{\nabla} \cdot \left[T^{2/3}\left(\boldsymbol{\nabla} \boldsymbol{u} + (\boldsymbol{\nabla} \boldsymbol{u})^{\mathrm{T}}\right)\right], \tag{1a}$$

$$\frac{1}{T}\left(\frac{\partial Y}{\partial t} + \boldsymbol{u} \cdot \boldsymbol{\nabla} Y\right) = -\dot{\omega} + \frac{1}{Re\,Pr\,Le} \boldsymbol{\nabla} \cdot \left(T^{2/3} \boldsymbol{\nabla} Y\right), \tag{1b}$$

$$\frac{1}{T}\left(\frac{\partial T}{\partial t} + \boldsymbol{u} \cdot \boldsymbol{\nabla} T\right) = \Delta T \dot{\omega} + \frac{1}{Re\,Pr} \boldsymbol{\nabla} \cdot \left(T^{2/3} \boldsymbol{\nabla} T\right), \tag{1c}$$

$$0 = \Delta T \dot{\omega} + \frac{1}{Re\,Pr} \boldsymbol{\nabla} \cdot \left(T^{2/3} \boldsymbol{\nabla} T\right) - \boldsymbol{\nabla} \cdot \boldsymbol{u}, \tag{1d}$$

where $\dot{\omega} = Da\, Y T^{-1} \exp\left[Ze\left(1 + \Delta T^{-1}\right)\left[1 - (1 + \Delta T)\, T^{-1}\right]\right]$ is the reaction rate. The six dimensionless parameters that appear in (1) include the adiabatic temperature change ΔT, the Zeldovich number Ze, the Damköhler number Da, the Reynolds number Re, the Prandtl number Pr, and the Lewis number Le, which are all defined in Appendix A. In this study, we focus on how Le and Da influence the flame behavior and fix the other parameters to constant values of $Re = 1000$, $Pr = 0.7$, $Ze = 10$, and $\Delta T = 4$. These values are selected to qualitatively model a generic lean premixed laminar flame

burning in air, rather than to quantitatively match the model to any specific fuel or operating condition. However, provided the model assumptions are justified, the dimensionless parameters can be quantitatively deduced from experimental conditions or computations with more complex chemistry models in a straightforward way. For example, Re, Pr, and Le may all be inferred from the gas properties of the unburned mixture; ΔT may be determined from the adiabatic flame temperature of the mixture; and Da and Ze may be identified by matching an observed flame speed and thickness to the model parameters using either an analytical relationship (e.g. [31, Ch. 5]) or a one-dimensional flame calculation.

As a technical note, it should be pointed out that the strong statement of the governing equations given by (1) possesses an apparent singularity at $r = 0$ due to the properties of the Laplace operator in cylindrical coordinates. However, in practice, the numerical approach (described in Section 2.4) leverages a weak (integral) formulation of (1) that is non-singular on the axis [32, Ch. 18.3]. In the weak form, the apparent singularity is removed following (1) multiplication by r arising from the differential volume $dV = r\, d\theta dr dx$ and (2) projection of the problem onto an analytic function space.

2.3. Bifurcation Analysis

For ease of presentation, Equation (1) can be rewritten in the form,

$$\mathcal{M}\left(\boldsymbol{q}\right)\frac{\partial \boldsymbol{q}}{\partial t} + \mathcal{R}\left(\boldsymbol{q}\right) = 0, \tag{2}$$

where $\mathcal{M}$ is the mass operator, $\mathcal{R}$ is the steady residual operator, and $\boldsymbol{q} = (\boldsymbol{u}, Y, T, p)^{\mathrm{T}}$ is the state vector. Owing to the temporal and azimuthal invariance of the system and boundary conditions, the base states of this system are both steady and axisymmetric. Hence, the base solutions $\boldsymbol{q}_b(x, r)$ to (2) satisfy,

$$\mathcal{R}_0\left(\boldsymbol{q}_b\right) = 0, \tag{3}$$

where the subscript refers to the Fourier component of the operator – i.e., in this case, the axisymmetric (zero azimuthal wavenumber) component of the 3-D operator $\mathcal{R}$. Such solutions, whether stable or unstable, are identified via Newton iteration until $\|\mathcal{R}_0\| < 10^{-13}$ using the time-invariant linearized system,

$$\mathcal{J}_0\left(\boldsymbol{q}_b\right)\Delta\boldsymbol{q}_0 = \mathcal{R}_0\left(\boldsymbol{q}_b\right), \tag{4}$$

with updates $\boldsymbol{q}_b \leftarrow \boldsymbol{q}_b - \Delta\boldsymbol{q}_0$ where $\mathcal{J} = \partial\mathcal{R}/\partial\boldsymbol{q}$ is the steady Jacobian operator. Once such base states are identified at one point in the parameter space, they are then traced along the various parameters using the tangent predictor–Moore–Penrose corrector scheme presented in [33, Sec. 3.2.1], thereby allowing continuation around turning points and identification of unstable solution branches. This methodology therefore offers a distinct advantage over conventional time integration approaches, which cannot converge to unstable solutions.

The asymptotic stability of base states is determined from the eigenspectrum of the global linearized reactive flow system. Each eigenvalue is associated with a global eigenvector representing infinitesimal perturbations of the form,

$$\boldsymbol{q'}\left(x, r, \theta, t\right) \propto \hat{\boldsymbol{q}}_m\left(x, r\right) \exp\left[\left(\sigma + \mathrm{i}\omega\right) t + \mathrm{i}m\theta\right] + c.c. \tag{5}$$

where σ is the linear growth/decay rate, ω is the pulsation frequency, m is the azimuthal wavenumber, and *c.c.* denotes the complex conjugate. We note that since the base states are steady and axisymmetric, this form of the perturbation given by (5) does not imply any loss of generality associated with the so-called "BiGlobal" assumption [34]. The generalized eigenvalue problem governing the long time evolution of such disturbances is,

$$\left(\sigma + \mathrm{i}\omega\right) \mathcal{M}\left(\boldsymbol{q}_b\right) \hat{\boldsymbol{q}}_m + \mathcal{J}_m\left(\boldsymbol{q}_b\right) \hat{\boldsymbol{q}}_m = 0, \tag{6}$$

where $(\sigma + \mathrm{i}\omega)$ is the eigenvalue and $\hat{\boldsymbol{q}}_m$ is the global eigenvector. If $\max\sigma < 0$ for all wavenumbers m at a given $\boldsymbol{q}_b$, the state is linearly globally stable. Conversely, if $\max\sigma > 0$ for any m, the state is linearly globally unstable and will spontaneously express self-excited dynamics. For a review of the connections between the global stability analysis approach used here and classical local stability analysis techniques, we refer the reader to [35]. Thus, the critical (marginally stable) state consists of a $\boldsymbol{q}_b$, $\hat{\boldsymbol{q}}_m$ pair that simultaneously satisfy (3) and (6) with $\sigma = 0$. Such points represent local bifurcations that are identified to machine precision ($\sigma < 10^{-13}$) and traced along the neutral curves using the block Newton schemes presented in [33, Sec. 3.2.3] with a convergence tolerance of 10^{-13} on the norm of the residual.

2.4. Discretization and Numerics

The axisymmetric burner configuration described above is discretized using triangulations of the meridional plane and an azimuthal Fourier expansion. In order to properly resolve the flow and flame field without requiring

unnecessary computational effort, an adaptive meshing procedure is used where each meridional mesh is adapted specifically to the global solution at each distinct state using the `adaptmesh` function in FreeFEM [36] with a $\mathbb{P}_1$ interpolation error tolerance of 1%. For each mesh, FreeFEM is also used to project the system and flow variables onto a Taylor–Hood-type mixed finite element space, consisting of $\mathbb{P}_2$ spaces for $\boldsymbol{u}$, Y, T, and the corresponding momentum, species, and energy conservation equations (1a-1c), combined with a $\mathbb{P}_1$ space for p and the mass conservation equation (1d). For the chosen $\mathbb{P}_1$ interpolation accuracy threshold, this projection yields a state vector with approximately 5×10^5 to 10^6 degrees of freedom per azimuthal Fourier component depending on the flame shape. As indicated by the mesh convergence study presented in Appendix B, this error tolerance is sufficient to determine values for the critical parameters and flame length with up to four digits of precision. Following the abstraction of the operators and boundary conditions by FreeFEM, the resulting linear algebra objects are manipulated and solved in parallel using PETSc [37] and SLEPc [38]. On a laptop computer with six 4.8 GHz processors and 32 GB of memory, the wall clock time per Newton iteration is approximately 10-20 seconds, and convergence is typically achieved in fewer than 10 iterations.

3. Results and Discussion

3.1. Axisymmetric flame dynamics

We begin our analysis with a study of the axisymmetric flame behavior and postpone discussion of non-axisymmetric dynamics to §3.2.

3.1.1. Case of $Le = 1$

By varying the Damköhler number (i.e. the dimensionless ratio of the chemical timescale to the flow timescale) at unity Le and monitoring the flame length, $L_f = x|\dot{\omega}(x,0) = \max_x(\dot{\omega}(x,0))$, we compute the bifurcation diagram shown in figure 2, revealing three distinct branches of solutions that are stable to axisymmetric disturbances. These stable branches are connected by two unstable branches of saddle solutions. Additionally, visualizations of the flame are presented at various points along the bifurcation diagram using streamlines to show the velocity field, heat release rate contours to show the reaction zone, and contours of the flame indicator $Y(T-1)$ to show the preheat zone. The diagram shows that steady conical flames (points 3 and 4) exist over a relatively limited interval of intermediate Damköhler

number. As Da is decreased, the chemical timescale becomes slower relative to the flow timescale, elongating the flame and weakening its anchor. At a certain critical value ($Da = 2.459 \times 10^3$ for the chosen parameters), the chemistry becomes too slow for the flame to maintain a kinematic balance with the flow, and a saddle–node bifurcation occurs. For Da smaller than this critical value, a solution corresponding to a steady conical flame does not exist – such an initial condition spontaneously undergoes axisymmetric blow-off. Conversely, as Da is increased, the flame speed becomes comparatively fast, and the solution eventually experiences a saddle–node bifurcation associated with spontaneous axisymmetric flash-back at $Da = 11.91 \times 10^3$.

This dynamics is qualitatively consistent with the seminal observations of Lewis and von Elbe [39], who studied the stability limits of burner-stabilized laminar premixed natural gas flames ($Le \approx 1$) under variations in flow rate and fuel mixture fraction. Their results can be related to ours by recognizing that varying the flow rate corresponds to a proportional variation of Re and an inversely proportional variation of Da (see Table A.2). However, a direct comparison is not possible since achieving an adiabatic flame temperature of $\Delta T = 4$ from room temperature natural gas would require a fuel percentage $\approx 4.5\%$ (i.e. an equivalence ratio ≈ 0.53), which is below the lean flammability limit identified in their study.

In addition to this limited steady branch of conical flame solutions, the bifurcation diagram also reveals two other equilibrium solutions that are stable to axisymmetric disturbances. First, since the system is well-posed at $Da = 0$, it possesses a nontrivial solution in this limit associated with a nonreacting jet. This branch of solutions continues to exist as Da is increased, where it represents an "un-ignited" (or "post-blow-off") state (thick blue curve and point 1 in figure 2). This state physically corresponds to an unlit burner, where L_f is not well-defined. As such, no numerical value of L_f could be reported and solutions are instead plotted in a gray shaded region on Figure 2. The un-ignited solution exists for a very large, but finite, range of Da in this system. This is because, despite the reaction's exponential dependence on temperature, for large enough Da values, the reaction proceeds sufficiently rapidly to induce autoignition. The mechanics of this autoignition process is not expected to be well-captured by the simple 1-step reaction chosen, but the overall implication is physically valid: nonreacting flow cannot be sustained as $Da \to \infty$. Instead, a saddle–node bifurcation must occur at a high Da value (not determined in this study – hence the gray shading in Figure 2), where the un-ignited solution curve folds onto an unstable

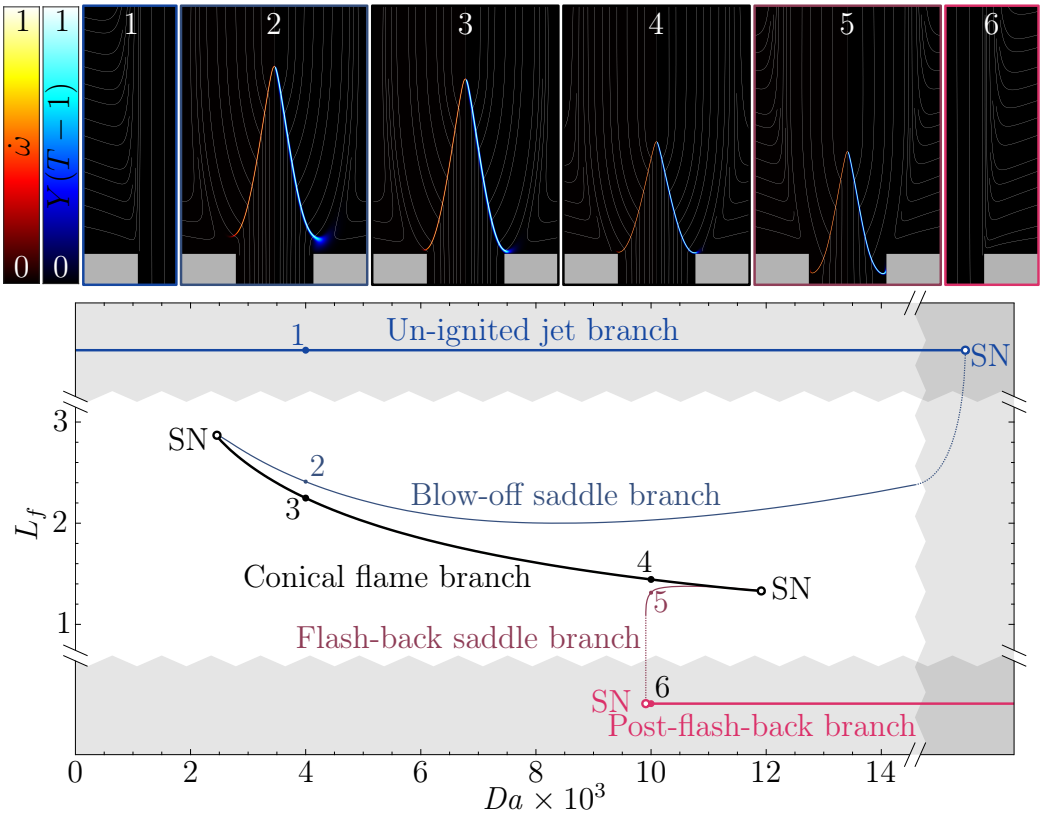

Figure 2: Bifurcation diagram for the $Le = 1$ system with streamline visualizations and heat release rate and flame indicator contours (both scaled to vary from 0 to 1) illustrating the axisymmetric flame shape at various points along the curve. Stable (saddle) branches are indicated by thick (thin) lines, and saddle–node (SN) bifurcation points are labeled.

solution branch (thin dark blue curve). Physically, this saddle branch, which is unstable to infinitesimal axisymmetric perturbations, delimits a tipping point for axisymmetric blow off that divides the basins of attraction of the conical flame and un-ignited jet solutions. For example, depending on the perturbation, an initial condition corresponding to the saddle flame indicated at point 2 may stabilize by propagating upstream until it reaches the stable conical flame state 3, or it may blow off to reach state 1.

Second, in the $Da \to \infty$ limit, the reaction cannot be prevented and occurs instantly along the domain inlet. This solution branch (thick red curve in figure 2) persists as Da decreases from infinity, where it represents a "post-flash-back" state stabilized by the Dirichlet conditions on the inlet reactant

mass fraction. In this case, the solution possesses well-defined negative L_f values, but these values are not reported quantitatively in Figure 2 since the post-flash-back branch is not a focus of this study. The post-flash-back state depends upon chemistry and cannot exist at $Da = 0$. Consequently, the post-flash-back state undergoes a saddle–node bifurcation at a minimum Da value of $Da = 9.906 \times 10^3$. At this bifurcation point, the flame in the "post-flash-back" solution can no longer be stabilized along the inlet and undergoes spontaneous blow-out towards a burner-stabilized flame. The bifurcation associated with blow-out of the post-flash-back flame state and the bifurcation associated with flash-back of the conical flame state are connected by an intermediate saddle branch (thin dark red curve) that separates the basins of attraction for the conical flame and post-flash-back solutions. For example, in a similar manner to the blow-off saddle, an infinitesimal axisymmetric perturbation to the flash-back saddle flame at point 5 could tip the system back to the stable conical flame at point 4 or trigger flash-back to the state at point 6.

3.1.2. Case of $Da = 4000$

We now consider the effect of varying Lewis number (i.e. the dimensionless ratio of the mixture's thermal diffusivity to the deficient reactant's mass diffusivity) at constant $Da = 4000$. Representative flame visualizations from these results are presented in Figure 3. In agreement with earlier experiments and computations, we find that the Lewis number has a profound effect on the steady, axisymmetric flame shapes. Owing to the effect of differential diffusion, $Le < 1$ mixtures (e.g. points 7 and 8) experience enhanced burning near the flame foot, where the flame is convex towards the reactants, while $Le > 1$ mixtures (e.g. point 9) favor burning at the concave flame tip [40, 41]. These Le-dependent, curvature-sensitive changes in reactant consumption and heat release yield local burning rate preferences along the curved flame front that drive the observed changes in the overall flame structure.

Figure 3 also illustrates the dynamics of the steady flame under varying Le. As in §3.1.1, the results reveal three branches of axisymmetric-stable solutions associated with the un-ignited jet, conical flame, and post-flash-back states. However, compared to the case of $Le = 1$ and varying Da considered previously, the mechanisms governing the relationships among these branches are distinct in the case of fixed Da and varying Le. The first and most obvious difference is that the un-ignited branch is completely disconnected from

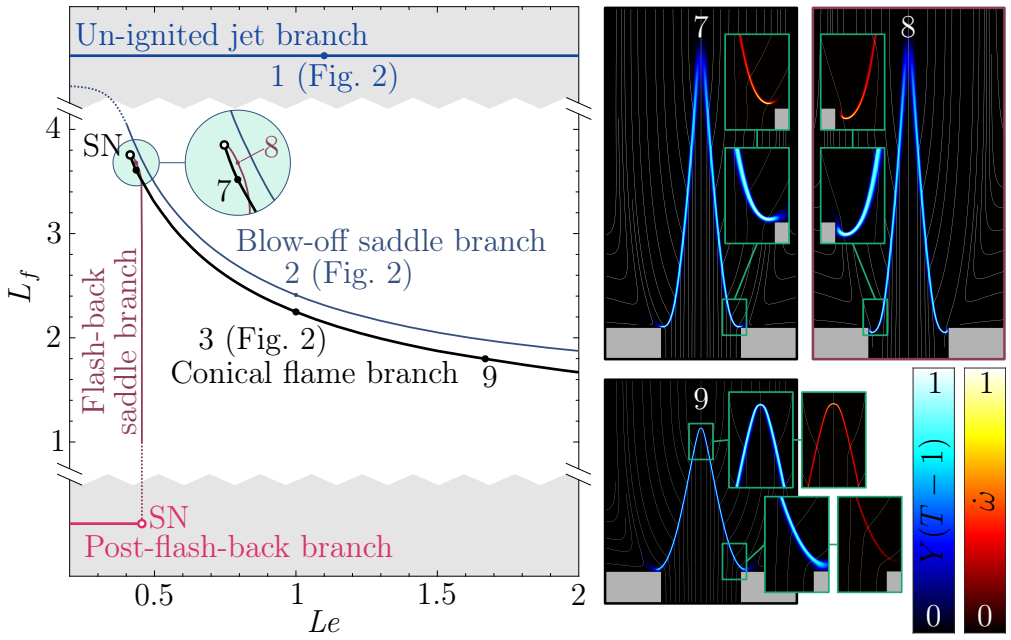

Figure 3: Bifurcation diagram for the $Da = 4000$ system with streamline visualizations and flame indicator and heat release rate contours (both scaled to vary from 0 to 1) illustrating the axisymmetric flame shape at various points along the curve. Stable (saddle) branches are indicated by thick (thin) lines, and saddle–node (SN) bifurcation points are labeled.

the other solution branches at this Damköhler number and exists for all Lewis numbers. Hence, for the chosen Da, there is no Le associated with spontaneous blow-off. Second, the conical flame solution branch encounters a saddle–node bifurcation corresponding to flash-back as the Lewis number decreases. As discussed in the previous paragraph, this dynamics physically originates from the flame curvature near the wall at the base of the flame, which leads to locally enhanced burning at sub-unity Lewis numbers. At the critical $Le = 0.4144$, the resulting stretched flame speed matches the local flow velocity in the laminar boundary layer, resulting in spontaneous flash-back. This stretch-coupled flash-back mechanism under varying Le should be contrasted to the flash-back situation described in §3.1.1, which precipitates when Da variations sufficiently accelerate the global burning rate independently of flame stretch. Visualizations of the flame shape via contours of $\dot{\omega}$ at the node (7) and saddle (8), which are, respectively, stable and unstable to axisymmetric disturbances, are included in figure 3 to illustrate this explanation.

Finally, we remark that our analysis considered a range of Le far greater than what is shown in Figure 3, though no interesting dynamics were identified for $Le > 2$ for the chosen parameters. In particular, our eigenvalue calculations did not detect any evidence of an axisymmetric pulsating flame instability at high Le. Rather, the transport of Y in (1b) becomes completely advection-dominated in the high-Le limit, and the flame length asymptotically approaches a constant value of $L_f \approx 0.8$.

3.2. Non-axisymmetric flame behavior

Having characterized the Bunsen burner system's axisymmetric dynamics, our main results focus on capturing and characterizing the symmetry-breaking phenomena observed in experiments. To this end, three-dimensional linear stability calculations are performed along the conical flame solution branches described in §3.1. These calculations reveal unstable eigenvalues for many m values over a significant portion of the parameter space. All of the identified unstable eigenvalues are found to be purely real (i.e. $\omega = 0$), meaning that they are associated with unstable, non-oscillatory, non-axisymmetric eigenmodes. Rather than studying the properties of these unstable eigenmodes, which cannot be correctly described in a linear framework due to nonlinear effects, our study will instead focus on describing the properties of their critical points ($\sigma = 0$), where the assumption of linearity is still justified. For such stationary eigenmodes with zero frequency and $\pm m$ azimuthal periodicities, the critical points represent circle–pitchfork (CP) bifurcations, i.e. zero-frequency Hopf bifurcations. (Note that, for systems such as ours in the O(2) symmetry group, zero-frequency Hopf bifurcations are analogous to pitchfork bifurcations with continuous rotational symmetry.)

Once identified, these CP bifurcation points are then traced within the Da–Le plane to define neutral CP curves that divide the parameter space into stable and unstable regions. These critical curves are presented in Figure 4 alongside the SN curves associated with the spontaneous blow-off and flashback events discussed in §3.1. The resulting stability map reveals that the steady conical flame spontaneously loses its axisymmetry through CP bifurcations associated with a range of $|m|$ values as the Lewis number decreases or as the Damköhler number increases. Further, these non-axisymmetric dynamics appear at parameter values within the limits identified for axisymmetric flashback. As detailed below, the primary instability for $Le \lesssim 1$ is associated with large $|m|$ values, leading to the spontaneous formation of polyhedral deformations along the flame front. Conversely, for $Le \gtrsim 1$, the

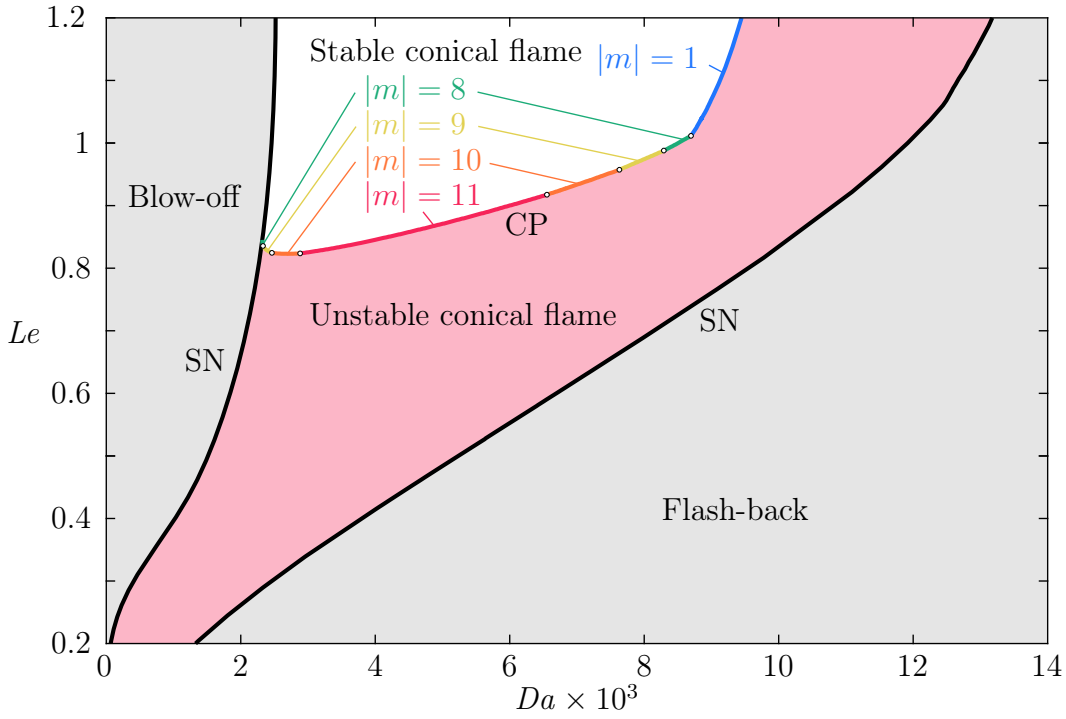

Figure 4: Stability map summarizing the dynamics of the conical flame in the *Da*–*Le* plane.

primary instability is associated with $|m| = 1$, leading to a spontaneous tilting of the flame along a particular direction.

These results suggest that symmetry breaking is a prominent characteristic of premixed conical flames as the limits for axisymmetric flash-back are approached. Hence, standalone axisymmetric analyses such as the one performed in §3.1 are generally insufficient for describing flash-back dynamics of Bunsen flames unless three-dimensional behavior can be ruled out.

3.2.1. Polyhedral Flames

Figure 4 illustrates that, for the chosen parameters, a loss of axisymmetry through CP bifurcations characterized by $|m| \geq 8$ appears for $Le \lesssim 1.01$. Here, we focus on the representative case of $Da = 4000$, where the critical Lewis number for the onset of three-dimensional behavior is $Le = 0.8454$, and the wavenumber of the associated CP bifurcation is $|m| = 11$. Nonetheless, Figure 5 indicates that $|m| = 11$ is just the first of many wavenumbers to become unstable as Le decreases. The exact critical values of Le and $|m|$

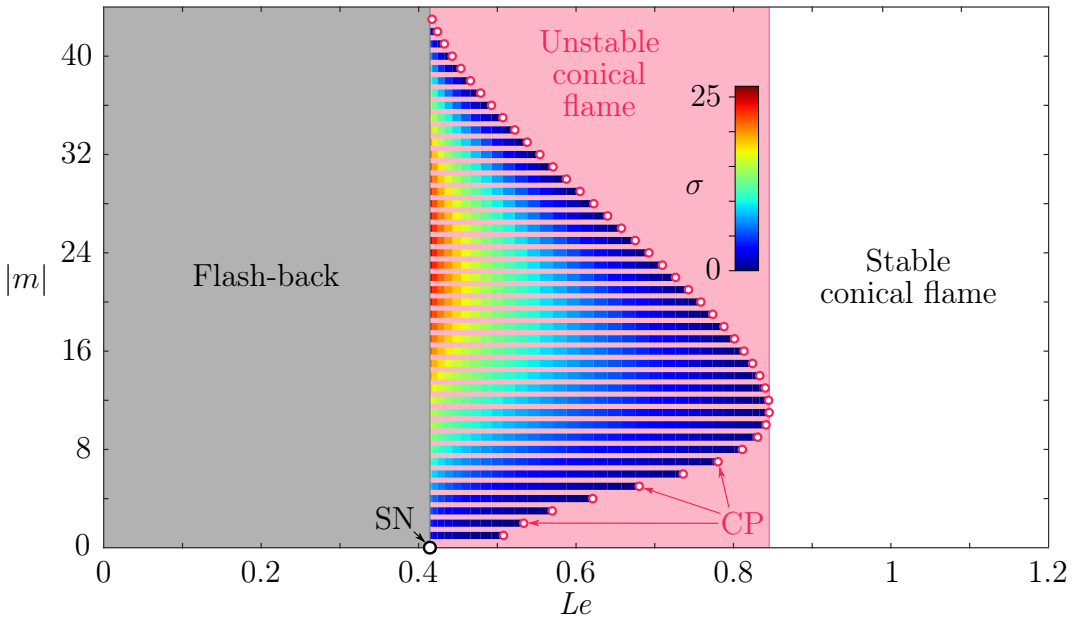

Figure 5: Bifurcation diagram at $Da = 4000$ showing the critical points, growth rates, and azimuthal wavenumbers associated with the bifurcating steady modes under varying Le. Here, CP and SN respectively denote circle–pitchfork and saddle–node bifurcation points.

differ across Da, but the qualitative trend that the primary instability is triggered by a CP bifurcation of moderate wavenumber, followed by further CP bifurcations with lower and higher $|m|$, remains consistent across Da for all $Le \lesssim 1$. This behavior is consistent with physical intuition derived from the classical dispersion relation for free flat flames, where the destabilizing role of differential diffusion at small scales makes the critical wavenumber relatively large for $Le < 1$ [5, 12]. Unlike the qualitative wavenumber scalings that follow from the analytic dispersion relation for a flat flame (for example, see the recent analysis of Weng *et al.* [22, Fig. 5a]), however, the present model enables quantitative predictions of which azimuthal wavenumbers may be unstable for a conical flame associated with a given set of parameters.

Though sub-unity Le certainly promote polyhedral flame instabilities, since Figure 4 identifies a leading CP bifurcation with $|m| = 8$ even at and slightly above $Le = 1$, the thermal-diffusive mechanism is certainly not the only contributor to destabilization of small scales. Further, such behavior cannot be attributed to any destabilization from flame stretch [9] or heat loss [10, 11], as both are insignificant at $Le = 1$ with single-step chemistry.

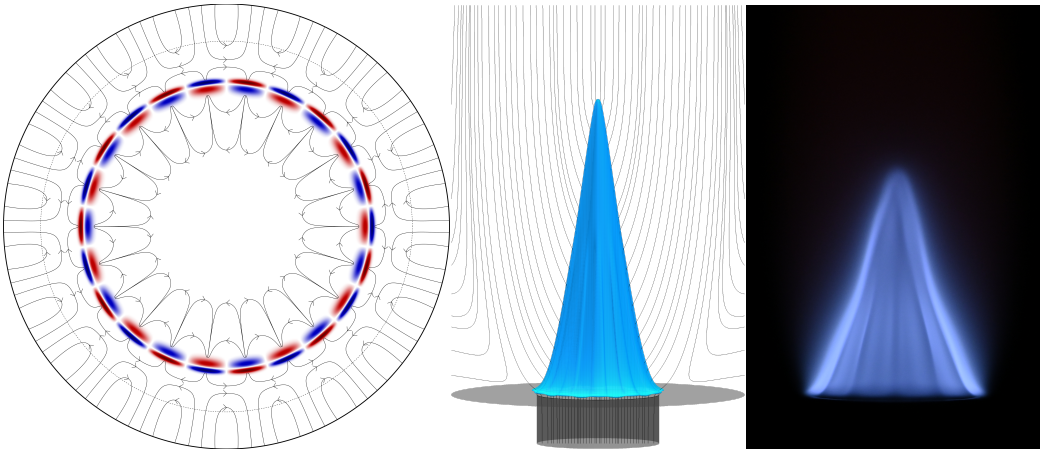

Figure 6: (left) Planar visualization of the critical eigenmode's in-plane streamlines and $[Y(T-1)]'$ contours at $x = 0.25$, (center) linear approximation of the computed $|m| = 11$ polyhedral flame structure via three-dimensional isosurface of $Y(T-1)$ at $(Da, Le) = (4000, 0.8454)$, and (right) experimental photograph of a similar polyhedral flame provided by Lulic et al. [21].

Rather, these $Le \approx 1$ results emphasize that the hydrodynamic mechanism plays an important role in the growth of polyhedral flame structures.

Examination of the critical $|m| = 11$ eigenmode reveals that the CP bifurcation corresponds to the emergence of a stationary (i.e., non-rotating) azimuthal deformation of the conical flame. As shown in Figure 6, the three-dimensional mode structure indicates the formation of 11 elongated ridges distributed azimuthally along the flame front. Visualization of the resulting polyhedral flame's approximate structure based on the superposition of the critical state and its critical eigenmode at arbitrary amplitude is also provided in Figure 6. This approximation does not account for nonlinear distortions resulting from the finite amplitude of the three-dimensional structure. For qualitative comparison, a photograph from the experimental work of Lulic *et al.* [21] is also shown for a polyhedral Bunsen flame produced by a 50/50 vol% CH_4/H_2 fuel mixture at an equivalence ratio of 0.8 and an initial temperature of 300 K. In terms of the dimensionless parameters used in our study, this experimental condition correlates to $Le = 0.859$, $\Delta T = 5.80$, $Ze = 8.54$, $Re = 8.28 \times 10^3$, $Da \approx 1.99 \times 10^4$, and $Pr = 0.701$. Note that, since their work is experimental, the Damköhler number has been estimated based on the flame speed and other parameters using Williams' analytical flame speed relation [31, Ch. 5.3, Eq. 75]. The other parameters are either given explic-

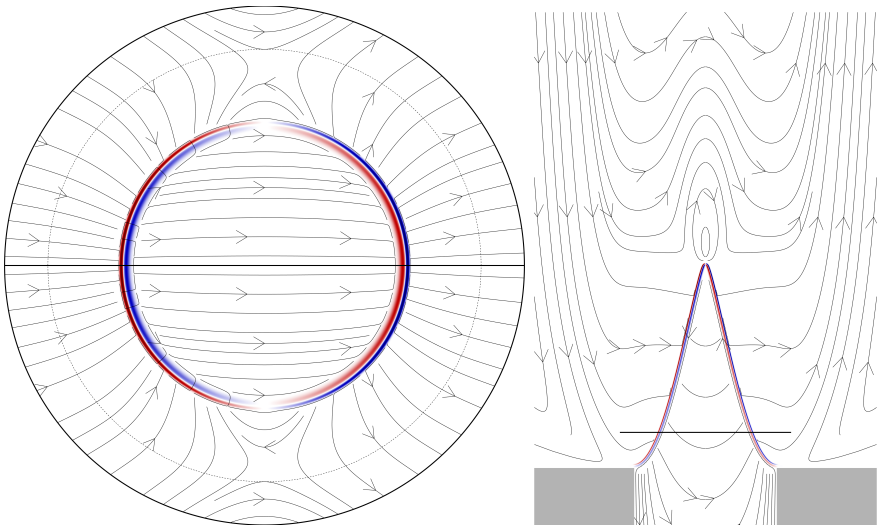

Figure 7: Visualizations of the critical $|m| = 1$ perturbation associated with the tilted flame CP bifurcation at $(Da, Le) = (9129, 1.1)$ via contours of $[Y(T-1)]'$ and projected streamlines within (left) the $x = 0.25$ axial slice plane and (right) the meridional plane of reflective symmetry. The horizontal black lines in the right (left) panel indicates the location of the axial (meridional) slice plane.

itly by Lulic *et al.* or are determined from the properties of the gas mixture. Hence, this experimental case has a significantly higher flame temperature and Reynolds number than our study, and the reaction parameters are different. Nonetheless, the striking resemblance in terms of the flame length, the wrinkle pattern, and Lewis number suggests that our model captures all of the physical elements necessary for describing polyhedral flames.

3.2.2. Tilted Flames

In contrast to the case of $Le \lesssim 1$, where symmetry breaking is associated with a range of relatively high wavenumbers, Figure 4 indicates that, within the chosen set of parameters, symmetry breaking for $Le > 1.01$ is triggered by CP bifurcation with $|m| = 1$. As such, this bifurcation does not manifest a polyhedral flame (which must have at least $|m| = 3$ faces along the reaction front), but instead evinces a "tilted flame" that is asymmetrically slanted along one meridional plane as shown in Figure 7. Here, we investigate the case of $Le = 1.1$, which is qualitatively representative of other super-unity Lewis numbers.

Figure 8 shows that $|m| = 1$ is the first wavenumber to destabilize as

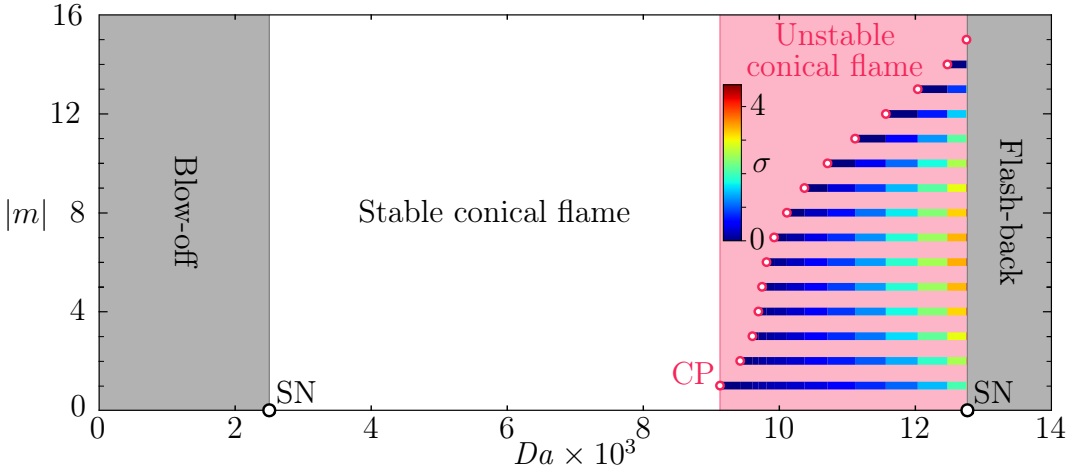

Figure 8: Bifurcation diagram at $Le = 1.1$ showing the critical points, growth rates, and azimuthal wavenumbers associated with the bifurcating steady modes under varying Da.

Da increases, but not the only one. The same is also true at higher Lewis numbers not shown in Figure 4. However, the range of higher wavenumbers that actually bifurcate from the conical flame solution branch is significantly smaller than was observed for $Le < 1$ in §3.2.1. This behavior may be attributed to the stabilizing role of differential diffusion at small scales for $Le > 1$, which exerts a strong selective effect on the wavenumbers that may be amplified by other mechanisms [5, 12]. In other words, since the $|m| = 1$ periodicity has the longest azimuthal wavelength, it is the first to bifurcate because it is the least damped by thermal-diffusive effects at the critical point.

4. Conclusion

A bifurcation analysis of premixed laminar conical flames, with varying Damköhler and Lewis numbers, has allowed us to retrieve the occurrence of flash-back, blow-off and symmetry breaking. The analysis is based on a system of equations that models three-dimensional reacting flow in the limit of vanishing Mach number, in a dimensionless formulation where the Damköhler number, the Lewis number, and four other physical control parameters can be varied independently from one another. Such a formulation facilitates the discussion of the influence of characteristic flame and flow properties, such as flame speed, flame thickness, and reactant diffusivity, as opposed to ex-

periments or dimensional simulations with detailed chemistry models, where it is usually difficult or impossible to vary one parameter without changing others.

The model yields steady conical flame states over a finite range of the Damköhler number, limited by blow-off below one critical value of Da, and by flash-back above another higher critical value. This model prediction is fully consistent with the expected behavior of real axisymmetric Bunsen flames. For unity Lewis number, and with a fixed choice of all other parameters, the limits in Da of the conical anchored flame regime have been quantified. It has further been shown that the end points of this regime are connected, via saddle branches, to two distinct families of axisymmetric flow solutions, which represent the post-blow-off and the post-flash-back steady states.

The most important result of the present analysis is the identification of three-dimensional instabilities, which are predicted to grow in conical steady flames at sufficiently low Lewis number or sufficiently high Damköhler number. At a fixed Damköhler number, this destabilization is therefore the direct result of differential diffusion, as it exists in hydrogen flames. The link between experimental and numerical observations of polyhedral flame shapes and low Lewis number has been made before using isothermal flame models based on the Kuramoto–Sivashinsky equation in one or two spatial dimensions. However, the shapes are shown here for the first time to arise as global linear instabilities that break the axisymmetry of a three-dimensional conical flame described by the low-Mach number reacting Navier–Stokes equations. In agreement with earlier experimental works, we find such instabilities to occur as the Lewis number drops below a critical value, thereby indicating the destabilizing role of thermal–diffusive mechanism at sub-unity Lewis number. However, our results also reveal that, with sufficiently high Da, instability can appear even for $Le \geq 1$. This highlights that the hydrodynamic mechanism can be sufficient to trigger the growth of polyhedral or asymmetric flame structures even without differential diffusion. In any case, the instability follows from a circle–pitchfork type bifurcation, which means that the resulting non-axisymmetric flame shape is again steady, at least as long as the amplitude of the instability remains small. Determining the amplitude-saturated non-axisymmetric flame shape, and eventually its rotation, as reported from experiments, will require further three-dimensional nonlinear analysis. Nonetheless, the findings show that symmetry breaking prior to flame flash-back is a notable behavior of conical flames, even for thermodiffusively stable reactant mixtures. As such, future characterizations

of conical flame behaviors should rule out any symmetry-breaking behaviors before adopting a strictly axisymmetric computational framework.

Declaration of Competing Interest

The authors declare that they have no known competing financial interests or personal relationships that could have appeared to influence the work reported in this paper.

Acknowledgements

The authors are grateful to Arne Scholtissek and the authors of [21] for graciously sharing their experimental images of polyhedral Bunsen flames. This project has received funding from the European Union's Horizon 2020 research and innovation programme under the Marie Skłodowska–Curie grant agreement No. 899987.

Appendix A. Derivation of Governing Equations

The governing equations for reacting flows consist of mass, species, momentum, and energy conservation equations and equations of state. We begin by assuming a Newtonian mixture of thermally perfect gases and recall the equations from Table 1.8 of [30]. Following the approach taken in [42, Appendix A], a series of approximations are made to simplify these equations. First, the chemistry is modeled by a single-step, irreversible reaction with a rate determined by the Arrhenius law and limited by the most deficient reactant. Note that this assumption, which applies to very lean or very rich mixtures, eliminates the equivalence ratio parameter from the analysis. Second, Soret, Dufour, and pressure gradient diffusion effects are all neglected such that the diffusion velocity is determined directly from Fick's Law. Third, the products and reactants are assumed to have equal molecular weights, equal but temperature-dependent viscosity/diffusivity coefficients, and equal, constant heat capacities. A detailed explanation of these assumptions is given in [30, Ch. 2]. With these assumptions and no external forces or energy

sources/sinks, our dimensional governing equations are,

$$\frac{\partial \rho^\star}{\partial t^\star} + \boldsymbol{\nabla}^\star \cdot (\rho^\star \boldsymbol{u}^\star) = 0, \tag{A.1a}$$

$$\frac{\partial \rho^\star Y^\star}{\partial t^\star} + \boldsymbol{\nabla}^\star \cdot (\rho^\star \boldsymbol{u}^\star Y^\star) = -\mathcal{A}^\star \rho^\star Y^\star \exp\left(\frac{-E_a^\star}{R^\star T^\star}\right) + \boldsymbol{\nabla}^\star \cdot (\rho^\star \mathcal{D}^\star \boldsymbol{\nabla}^\star Y^\star), \tag{A.1b}$$

$$\frac{\partial \rho^\star \boldsymbol{u}^\star}{\partial t^\star} + \boldsymbol{\nabla}^\star \cdot (\rho^\star \boldsymbol{u}^\star \boldsymbol{u}^\star) = -\boldsymbol{\nabla}^\star p^\star + \boldsymbol{\nabla}^\star \cdot \boldsymbol{\tau}^\star, \tag{A.1c}$$

$$\frac{\partial \rho^\star E^\star}{\partial t^\star} + \boldsymbol{\nabla}^\star \cdot (\rho^\star \boldsymbol{u}^\star E^\star) = \Delta h_c^\star \mathcal{A}^\star \rho^\star Y^\star \exp\left(\frac{-E_a^\star}{R^\star T^\star}\right) + \boldsymbol{\nabla}^\star \cdot (k^\star \boldsymbol{\nabla}^\star T^\star + \boldsymbol{u}^\star \cdot \boldsymbol{\tau}^\star - \boldsymbol{u}^\star p^\star), \tag{A.1d}$$

$$p^\star = \rho^\star R^\star T^\star, \tag{A.1e}$$

$$e_s^\star = c_v^\star T^\star, \tag{A.1f}$$

$$\boldsymbol{\tau}^\star = \mu^\star \left(\boldsymbol{\nabla}^\star \boldsymbol{u}^\star + (\boldsymbol{\nabla}^\star \boldsymbol{u}^\star)^{\mathrm{T}}\right) + \left(\kappa^\star - \frac{2\mu^\star}{3}\right) \boldsymbol{I} (\boldsymbol{\nabla}^\star \cdot \boldsymbol{u}^\star), \tag{A.1g}$$

where stars are used to denote dimensional variables. Here, $\rho^\star$ is the density, $\boldsymbol{u}^\star$ is the velocity vector, $Y^\star$ is the mass fraction of the deficient species, $\mathcal{A}^\star$ is the Arrhenius frequency factor, $E_a^\star$ is the Arrhenius activation energy, $R^\star$ is the specific gas constant, $T^\star$ is the temperature, $\mathcal{D}^\star$ is the species mass diffusivity, $p^\star$ is the static pressure, $E^\star = e_s^\star + \frac{1}{2}\boldsymbol{u}^\star \cdot \boldsymbol{u}^\star$ is the sum of the specific sensible energy e_s and specific kinetic energy, $\Delta h_c^\star$ is the specific enthalpy of combustion, $k^\star$ is the thermal conductivity, $c_v^\star$ is the mixture specific heat at constant volume, $\mu^\star$ is the total dynamic shear viscosity, and $\kappa^\star$ is the total second (volume) viscosity.

To further simplify, the dimensional variables that have been used in the previous equations are scaled by the reference properties of the reactants at the inlet (subscript R) and the velocity and length scale of the flow ($U^\star$ and $D^\star$, respectively, see §2.1). These reference quantities are chosen such that the dimensionless quantities remain $O(1)$ for a Mach number defined by $M \equiv U^\star \sqrt{\rho_R^\star} / \sqrt{\gamma p_R^\star}$ (where $\gamma = \frac{c_p^\star}{c_v^\star}$ is the specific heat ratio). The scaled,

dimensionless quantities are defined by

$$\rho = \frac{\rho^\star}{\rho_R^\star},\ Y = \frac{Y^\star}{Y_R^\star},\ \boldsymbol{u} = \frac{\boldsymbol{u}^\star}{U^\star},\ E = \frac{\rho_R^\star E^\star}{p_R^\star},\ p = \frac{p^\star}{p_R^\star},\ T = \frac{T^\star}{T_R^\star},$$
$$\boldsymbol{x} = \frac{\boldsymbol{x}^\star}{D^\star},\ t = \frac{U^\star t^\star}{D^\star}, \boldsymbol{\tau} = \frac{D^\star \boldsymbol{\tau}^\star}{\mu_R^\star U^\star},\ \mu = \frac{\mu^\star}{\mu_R^\star},\ \kappa = \frac{\kappa^\star}{\mu_R^\star},\ \mathcal{D} = \frac{\mathcal{D}^\star}{\mathcal{D}_R^\star},\ k = \frac{k^\star}{k_R^\star}.$$

Note that, with this normalization, the constant specific heats are given by $c_p = \gamma/(\gamma-1)$ and $c_v = 1/(\gamma-1)$. Substituting these definitions into (A.1) yields the dimensionless equations,

$$\frac{\partial \rho}{\partial t} + \boldsymbol{\nabla}\cdot(\rho\boldsymbol{u}) = 0, \tag{A.2a}$$

$$\frac{\partial \rho Y}{\partial t} + \boldsymbol{\nabla}\cdot(\rho\boldsymbol{u}Y) = -B\rho Y \exp\left(\frac{-T_a}{T}\right) + \frac{1}{RePrLe}\boldsymbol{\nabla}\cdot(\rho\mathcal{D}\boldsymbol{\nabla}Y), \tag{A.2b}$$

$$\frac{\partial \rho\boldsymbol{u}}{\partial t} + \boldsymbol{\nabla}\cdot(\rho\boldsymbol{u}\boldsymbol{u}) = -\frac{1}{\gamma M^2}\boldsymbol{\nabla}p + \frac{1}{Re}\boldsymbol{\nabla}\cdot\boldsymbol{\tau}, \tag{A.2c}$$

$$\frac{\partial \rho E}{\partial t} + \boldsymbol{\nabla}\cdot(\rho\boldsymbol{u}E) = \frac{\gamma B\Delta T}{\gamma-1}\rho Y \exp\left(\frac{-T_a}{T}\right) + \boldsymbol{\nabla}\cdot\left(\frac{\gamma k}{(\gamma-1)RePr}\boldsymbol{\nabla}T + \frac{\gamma M^2}{Re}\boldsymbol{u}\cdot\boldsymbol{\tau} - \boldsymbol{u}p\right), \tag{A.2d}$$

$$p = \rho T, \tag{A.2e}$$

$$e_s = \frac{T}{\gamma-1}, \tag{A.2f}$$

$$\boldsymbol{\tau} = \mu\left(\boldsymbol{\nabla}\boldsymbol{u} + (\boldsymbol{\nabla}\boldsymbol{u})^{\mathrm{T}}\right) + \left(\kappa - \frac{2\mu}{3}\right)\boldsymbol{I}(\boldsymbol{\nabla}\cdot\boldsymbol{u}), \tag{A.2g}$$

where the following dimensionless parameters have been defined: the Arrhenius pre-exponential factor, $B \equiv \mathcal{A}^\star D^\star/U^\star$; the adiabatic temperature change, $\Delta T \equiv Y_R^\star \Delta h_c^\star/(c_{p,R}^\star T_R^\star)$; the Arrhenius activation temperature, $T_a \equiv E_a^\star/(R^\star T_R^\star)$; the Prandtl number, $Pr \equiv c_{p,R}^\star \mu_R^\star/k_R^\star$; the Lewis number, $Le \equiv k_R^\star/(\rho_R^\star c_{p,R}^\star \mathcal{D}_R^\star)$; the Reynolds number, $Re \equiv \rho_R^\star U^\star D^\star/\mu_R^\star$. Note that the Mach number also appears in the dimensionless non-chemical energy, where $E = e_s + \frac{1}{2}\gamma M^2 \boldsymbol{u}\cdot\boldsymbol{u}$.

To derive the low-Mach number form of the equations, each flow variable is expanded in orders of the Mach number, i.e.

$$\psi = \psi_{(0)} + M\psi_{(1)} + M^2\psi_{(2)} + O(M^3). \tag{A.3}$$

Here, ψ represents an arbitrary flow variable. Substituting the asymptotic expansion (A.3) into (A.2) and collecting only the equations which do not vanish in the limit of zero Mach number yields,

$$\frac{\partial \rho_{(0)}}{\partial t} + \boldsymbol{\nabla} \cdot \left(\rho_{(0)} \boldsymbol{u}_{(0)}\right) = 0, \tag{A.4a}$$

$$\frac{\partial \rho_{(0)} Y_{(0)}}{\partial t} + \boldsymbol{\nabla} \cdot \left(\rho_{(0)} \boldsymbol{u}_{(0)} Y_{(0)}\right) = -B \rho_{(0)} Y_{(0)} \exp\left(\frac{-T_a}{T_{(0)}}\right) + \frac{1}{RePrLe} \boldsymbol{\nabla} \cdot \left(\rho_{(0)} \mathcal{D}_{(0)} \boldsymbol{\nabla} Y_{(0)}\right), \tag{A.4b}$$

$$0 = -\boldsymbol{\nabla} p_{(0)}, \tag{A.4c}$$

$$\frac{\partial \rho_{(0)} \boldsymbol{u}_{(0)}}{\partial t} + \boldsymbol{\nabla} \cdot \left(\rho_{(0)} \boldsymbol{u}_{(0)} \boldsymbol{u}_{(0)}\right) = -\boldsymbol{\nabla} p_{(2)} + \frac{1}{Re} \boldsymbol{\nabla} \cdot \boldsymbol{\tau}_{(0)}, \tag{A.4d}$$

$$\frac{\partial \rho_{(0)} E_{(0)}}{\partial t} + \boldsymbol{\nabla} \cdot \left(\rho_{(0)} \boldsymbol{u}_{(0)} E_{(0)}\right) = \frac{\gamma B \Delta T}{\gamma - 1} \rho_{(0)} Y_{(0)} \exp\left(\frac{-T_a}{T_{(0)}}\right) + \boldsymbol{\nabla} \cdot \left(\frac{\gamma k_{(0)}}{(\gamma - 1) RePr} \boldsymbol{\nabla} T_{(0)} - \boldsymbol{u}_{(0)} p_{(0)}\right), \tag{A.4e}$$

$$p_{(0)} = \rho_{(0)} T_{(0)}, \tag{A.4f}$$

$$E_{(0)} = \frac{T_{(0)}}{\gamma - 1}, \tag{A.4g}$$

$$\boldsymbol{\tau}_{(0)} = \mu_{(0)} \left(\boldsymbol{\nabla} \boldsymbol{u}_{(0)} + \left(\boldsymbol{\nabla} \boldsymbol{u}_{(0)}\right)^{\mathrm{T}}\right) + \left(\kappa_{(0)} - \frac{2\mu_{(0)}}{3}\right) \boldsymbol{I} \left(\boldsymbol{\nabla} \cdot \boldsymbol{u}_{(0)}\right). \tag{A.4h}$$

Upon examination of (A.4), it is apparent that the $O(M^{-2})$ momentum equation (A.4c), constrains the leading-order pressure to be spatially uniform. Using the equation of state (A.4f), this requires that the product $\rho_{(0)} T_{(0)}$ must also be spatially uniform. With these constraints, $p_{(2)}$ now represents a hydrodynamic component of pressure that is fully decoupled from the spatially-uniform thermodynamic pressure at leading order in M. Additionally, the leading-order non-chemical energy must be directly proportional to the temperature. Applying these restrictions to (A.4) and dropping the subscripts denoting the expansion orders for all variables except the pressure

returns,

$$\frac{\partial \rho}{\partial t} + \boldsymbol{\nabla} \cdot (\rho \boldsymbol{u}) = 0, \tag{A.5a}$$

$$\frac{\partial \rho Y}{\partial t} + \boldsymbol{\nabla} \cdot (\rho \boldsymbol{u} Y) = -B \rho Y \exp\left(\frac{-T_a}{T}\right) + \frac{1}{RePrLe} \boldsymbol{\nabla} \cdot (\rho \mathcal{D} \boldsymbol{\nabla} Y), \tag{A.5b}$$

$$\frac{\partial \rho \boldsymbol{u}}{\partial t} + \boldsymbol{\nabla} \cdot (\rho \boldsymbol{u}\boldsymbol{u}) = -\boldsymbol{\nabla} p_{(2)} + \frac{1}{Re} \boldsymbol{\nabla} \cdot \left[\mu \left(\boldsymbol{\nabla} \boldsymbol{u} + (\boldsymbol{\nabla} \boldsymbol{u})^{\mathrm{T}} \right) + \left(\kappa - \frac{2\mu}{3} \right) \boldsymbol{I} (\boldsymbol{\nabla} \cdot \boldsymbol{u}) \right], \tag{A.5c}$$

$$\frac{1}{\gamma} \frac{\mathrm{d} p_{(0)}}{\mathrm{d} t} + p_{(0)} \boldsymbol{\nabla} \cdot \boldsymbol{u} = B \Delta T \rho Y \exp\left(\frac{-T_a}{T}\right) + \frac{1}{RePr} \boldsymbol{\nabla} \cdot (k \boldsymbol{\nabla} T), \tag{A.5d}$$

$$p_{(0)} = \rho T. \tag{A.5e}$$

In the open flow considered in our analysis, the thermodynamic pressure is subject to time-invariant boundary conditions. This necessitates that $p_{(0)}$ is everywhere identically one, which simplifies the energy equation (A.5d) and the equation of state (A.5e). A significant simplification to the viscous stress tensor in the momentum equation can also be realized by redefining the hydrodynamic pressure as $p = p_{(2)} - Re^{-1} (\kappa - 2\mu/3) (\boldsymbol{\nabla} \cdot \boldsymbol{u})$. This substitution is possible because the normal viscous stresses act along the gradient with the hydrodynamic pressure, and can thus be absorbed into the hydrodynamic pressure term without any other changes. Next, the numerical properties of the reaction rate terms are improved by defining the Damköhler number $Da = B \exp(-Ze(1 + \Delta T)/\Delta T)$ using the Zeldovich number $Ze = T_a \Delta T/(1 + \Delta T)^2$. This effective re-scaling of the pre-exponential factor does not change any physics of the model, but conveniently normalizes the exponential terms such that rounding errors due to finite-precision arithmetic do not significantly affect the floating-point numerics at high Zeldovich numbers. Finally, the temperature-dependencies of the dimensionless viscosity μ, the thermal conductivity k and mass diffusion coefficient $\rho\mathcal{D}$ are taken to be equal on the basis of Chapman–Enskog gas kinetic theory [43, Ch. 10], with a power law scaling of $T^{2/3}$. Incorporating these simplifications, (A.5) is reduced to (1). The final parameters that appear in (1) are summarized in Table A.2.

Appendix B. Mesh convergence study

This appendix assesses the robustness of the results to variations in computational mesh resolution. Additional computations were performed on

$$\begin{aligned}
\text{Adiabatic temperature change:} \quad \Delta T &= \frac{Y_R^\star \Delta h_c^\star}{c_{p,R}^\star T_R^\star} = \frac{T_{\text{ad}}^\star - T_R^\star}{T_R^\star} \\
\text{Zeldovich number:} \quad Ze &= \frac{E_a^\star \left(T_{\text{ad}}^\star - T_R^\star\right)}{R_u^\star \left(T_R^\star\right)^2} \\
\text{Damköhler number:} \quad Da &= \frac{\mathcal{A}^\star D^\star}{U^\star} \exp\left(-\frac{E_a^\star}{R_u^\star T_{\text{ad}}^\star}\right) \\
\text{Reynolds number:} \quad Re &= \frac{\rho_R^\star U^\star D^\star}{\mu_R^\star} \\
\text{Prandtl number:} \quad Pr &= \frac{\mu_R^\star c_{p,R}^\star}{k_R^\star} \\
\text{Lewis number:} \quad Le &= \frac{k_R^\star}{c_{p,R}^\star \rho_R^\star \mathcal{D}_R^\star}
\end{aligned}$$

Table A.2: Definitions of dimensionless parameters appearing in (1). Stars denote dimensional variables. Here, $T_{\text{ad}}^\star = T_R^\star + Y_R^\star \Delta h_c^\star / c_{p,R}^\star$ is the adiabatic flame temperature.

adapted meshes obtained with smaller $\mathbb{P}_1$ error tolerances equal to 0.5% and 0.3%. Since our results are discretized on second-order Taylor–Hood elements (see §2.4), these tolerances respectively correspond to solutions that are roughly four and ten times more accurate (and computationally intensive) than the reference solutions. In Table B.3, the new L_f values and critical parameter values obtained on these meshes are compared to the results given in §3. Based on the agreement across all cases, the 1% error tolerance is determined to be sufficient to retrieve accurate results with up to four significant digits of precision.

References

[1] D. Noble, D. Wu, B. Emerson, S. Sheppard, T. Lieuwen, L. Angello, Assessment of Current Capabilities and Near-Term Availability of Hydrogen-Fired Gas Turbines Considering a Low-Carbon Future, J. Eng. Gas Turb. Power 143 (2021).

[2] G. I. Sivashinsky, Instabilities, pattern formation, and turbulence in flames, Annu. Rev. Fluid Mech. 15 (1983) 179–199.

[3] M. Matalon, The Darrieus–Landau instability of premixed flames, Fluid Dyn. Res. 50 (2018) 051412.

Table B.3: Mesh convergence study results. Here, `err` is the $\mathbb{P}_1$ error tolerance, D.o.F. is the associated number of degrees of freedom of the Taylor–Hood finite element basis per azimuthal Fourier component, Criticality indicates the value of the indicated parameter at the bifurcation point, and L_f indicates the flame length at the critical point.

	`err`	**D.o.F.**	**Criticality**	$\boldsymbol{L_f}$
$Le = 1$: $m = 0$ SN	0.01	686 719	$Da = 2458.7$	2.8695
	0.005	1 278 670	$Da = 2458.6$	2.8692
	0.003	2 127 213	$Da = 2458.4$	2.8695
$Le = 1$: $m = 0$ SN	0.01	735 306	$Da = 11915.$	1.3306
	0.005	1 528 545	$Da = 11919.$	1.3302
	0.003	2 298 264	$Da = 11919.$	1.3302
$Da = 4000$: $m = 0$ SN	0.01	814 307	$Le = 0.41438$	3.7544
	0.005	1 241 803	$Le = 0.41433$	3.7551
	0.003	2 455 969	$Le = 0.41433$	3.7549
$Da = 4000$: $\lvert m\rvert = 11$ CP	0.01	735 593	$Le = 0.84536$	2.4442
	0.005	1 301 928	$Le = 0.84550$	2.4445
	0.003	2 305 019	$Le = 0.84559$	2.4438
$Le = 1.1$: $\lvert m\rvert = 1$ CP	0.01	724 064	$Da = 9129.1$	1.4360
	0.005	1 542 424	$Da = 9127.0$	1.4356
	0.003	2 299 418	$Da = 9119.1$	1.4363

[4] G. I. Barenblatt, Y. B. Zeldovich, A. G. Istratov, On diffusional-thermal stability of a laminar flame, Prik. Mekh. Tekh. Fiz. 3 (1962) 15–24.

[5] G. I. Sivashinsky, Diffusional-thermal theory of cellular flames, Combust. Sci. Technol. 15 (1977) 137–145.

[6] G. Darrieus, Propagation d'un front de flamme, La Technique Moderne 30 (1938) 18.

[7] L. D. Landau, On the theory of slow combustion, Acta Physicochim. (USSR) 19 (1944) 77–85.

[8] G. Markstein, Chapter b - theory of flame propagation, in: G. H. Markstein (Ed.), Nonsteady Flame Propagation, Vol. 75, Elsevier, 1964, pp. 5–14.

[9] C. Law, Dynamics of stretched flames, Symp. (Int.) Combust. 22 (1989) 1381–1402.

[10] G. Joulin, P. Clavin, Linear stability analysis of nonadiabatic flames: Diffusional-thermal model, Combust. Flame 35 (1979) 139–153.

[11] P. Clavin, C. Nicoli, Effect of heat losses on the limits of stability of premixed flames propagating downwards, Combust. Flame 60 (1985) 1–14.

[12] C. Altantzis, C. E. Frouzakis, A. G. Tomboulides, M. Matalon, K. Boulouchos, Hydrodynamic and thermodiffusive instability effects on the evolution of laminar planar lean premixed hydrogen flames, J. Fluid Mech. 700 (2012) 329–361.

[13] F. Creta, P. E. Lapenna, R. Lamioni, N. Fogla, M. Matalon, Propagation of premixed flames in the presence of Darrieus–Landau and thermal diffusive instabilities, Combust. Flame 216 (2020) 256–270.

[14] L. Berger, A. Attili, H. Pitsch, Synergistic interactions of thermodiffusive instabilities and turbulence in lean hydrogen flames, Combust. Flame 244 (2022) 112254.

[15] G. I. Sivashinsky, C. K. Law, G. Joulin, On stability of premixed flames in stagnation point flow, Combust. Sci. Technol. 28 (1982) 155–159.

[16] A. Smithells, H. Ingle, The structure and chemistry of flames, J. Chem. Soc., Trans. 61 (1892) 204–216.

[17] F. A. Smith, S. F. Pickering, Bunsen flames of unusual structure, Bur. Stand. J. Res. 3 (1929) 65–74.

[18] J. Garside, B. Jackson, The formation and some properties of polyhedral burner flames, Symp. (Int.) Combust. 4 (1953) 545–552.

[19] S. Sohrab, C. Law, Influence of burner rim aerodynamics on polyhedral flames and flame stabilization, Combust. Flame 62 (1985) 243–254.

[20] A. N. Jacobi, S. H. Sohrab, Chemical kinetic and thermal aspects of cellular premixed flames, Combust. Sci. Technol. 69 (1990) 17–32.

[21] H. Lulic, A. Breicher, A. Scholtissek, P. E. Lapenna, A. Dreizler, F. Creta, C. Hasse, D. Geyer, F. Ferraro, On polyhedral structures of lean methane/hydrogen bunsen flames: Combined experimental and numerical analysis, Proc. Combust. Inst. (2022).

[22] Y. Weng, A. Potnis, A. Saha, Regime and morphology of polyhedral bunsen flames, Combust. Flame 248 (2023) 112585.

[23] J. Buckmaster, Polyhedral flames—an exercise in bimodal bifurcation analysis, SIAM J. Appl. Math. 44 (1984) 40–55.

[24] D. O. Olagunju, B. J. Matkowsky, Polyhedral flames, SIAM J. Appl. Math. 51 (1991) 73–89.

[25] D. Michelson, Rotating bunsen flames as solutions of the kuramoto-sivashinsky equation, J. Dyn. Differ. Equ. 5 (1993) 375–415.

[26] A. G. Class, Rotating polyhedral flames, ZAMM - Z. Angew. Math. Me. 81 (2001) 783–784.

[27] S. Gutman, R. L. Axelbaum, G. I. Sivashinsky, On bunsen burner polyhedral flames, Combust. Sci. Technol. 98 (1994) 57–70.

[28] M. L. Frankel, An equation of surface dynamics modeling flame fronts as density discontinuities in potential flows, Phys. Fluids A: Fluid 2 (1990) 1879–1883.

[29] B. Denet, Nonlinear model equation for three-dimensional bunsen flames, Phys. Fluids 16 (2004) 1149–1155.

[30] T. Poinsot, D. Veynante, Theoretical and Numerical Combustion, 3rd Edition, T. Poinsot, 2011.

[31] F. Williams, Combustion Theory: The Fundamental Theory of Chemically Reacting Flow Systems, 2nd Edition, CRC Press, 1985.

[32] J. Boyd, Chebyshev and Fourier Spectral Methods: Second Revised Edition, Dover Books on Mathematics, Dover Publications, 2013.

[33] C. M. Douglas, B. L. Emerson, T. C. Lieuwen, Nonlinear dynamics of fully-developed swirling jets, J. Fluid Mech. (2021).

[34] M. P. Juniper, A. Hanifi, V. Theofilis, Modal Stability Theory: Lecture notes from the FLOW-NORDITA Summer School on Advanced Instability Methods for Complex Flows, Stockholm, Sweden, 2013, Applied Mechanics Reviews 66 (2) (2014) 024804. doi:10.1115/1.4026604.

[35] J.-M. Chomaz, Global instabilities in spatially developing flows: Non-normality and nonlinearity, Annual Review of Fluid Mechanics 37 (1) (2005) 357–392. doi:10.1146/annurev.fluid.37.061903.175810.

[36] F. Hecht, New development in freefem++, J. Numer. Math. 20 (3-4) (2012) 251–265.

[37] S. Balay, S. Abhyankar, M. F. Adams, J. B. P. Brune, K. Buschelman, L. Dalcin, A. Dener, V. E. W. D. Gropp, D. Kaushik, M. G. Knepley, D. A. M. L. C. McInnes, R. T. Mills, T. Munson, K. R. P. Sanan, B. F. Smith, S. Zampini, H. Zhang, H. Zhang, PETSc users manual, Tech. Rep. ANL-95/11 - Revision 3.13, Argonne National Laboratory (2020).

[38] V. Hernandez, J. E. Roman, V. Vidal, SLEPc: A scalable and flexible toolkit for the solution of eigenvalue problems, ACM Trans. Math. Software 31 (3) (2005) 351–362.

[39] B. Lewis, G. von Elbe, Stability and structure of burner flames, J. Chem. Phys. 11 (1943) 75–97.

[40] C. Wu, C. Law, On the determination of laminar flame speeds from stretched flames, Symp. (Int.) Combust. 20 (1985) 1941–1949.

[41] M. Mizomoto, H. Yoshida, Effects of lewis number on the burning intensity of bunsen flames, Combust. Flame 70 (1987) 47–60.

[42] C. M. Douglas, Dynamics of swirling jets and flames, Ph.D. thesis, School of Mechanical Engineering, Georgia Institute of Technology (5 2021).

[43] S. Chapman, T. G. Cowling, The Mathematical Theory of Non-Uniform Gases, 3rd Edition, Cambridge University Press, 1970.